Materials & Design 248 (2024) 113463

Contents lists available at ScienceDirect

Materials & Design

journal homepage: www.elsevier.com/locate/matdes

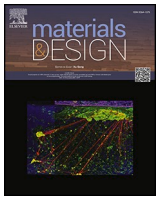

Optimizing α-tricalcium phosphate bone cement composite formulations: The critical role of bioactive glass particle size

Öznur Demir [a,b], Estere Oselska [a,b], Maris Bertins [c], Arturs Viksna [c], Aldo R. Boccaccini [d], Dagnija Loca [a,b,*]

[a] Institute of Biomaterials and Bioengineering, Faculty of Natural Sciences and Technology, Riga Technical University, Pulka St. 3, Riga LV-1007, Latvia
[b] Baltic Biomaterials Centre of Excellence, Headquarters at Riga Technical University, Riga, Latvia
[c] University of Latvia, Faculty of Medicine and Life Sciences, Jelgavas St. 1, Riga LV-1004, Latvia
[d] Institute of Biomaterials, University of Erlangen-Nuremberg, 91058 Erlangen, Germany

ARTICLE INFO

Keywords:
Calcium phosphate
Bioactive glass
Bone cements
Mesoporous
Bone regeneration
Particle size

ABSTRACT

Calcium phosphate cements (CPCs) have been extensively utilized as bone grafting material due to their inherent osteoconductive properties, although they often lacked sufficient biological performance for effective bone healing at the defect site. Incorporating mesoporous bioactive glass (MBG) into CPCs offers a solution by improving porosity, promoting degradation and increasing the available surface area. In the scope of this study, we integrated MBG into CPCs and assessed the impact of varying MBG particle sizes (<20 μm, <38 μm, <100 μm) on the setting characteristics, microstructure, mechanical strength, and preliminary cell response of CPCs. Investigations revealed that < 20 μm MBG particles significantly improved the setting characteristics and compressive strength of CPCs, while < 38 μm particles promoted degradation and ion release, facilitating apatite formation. MBG incorporation was found to promote microstructural homogeneity and facilitate apatite formation, with particle size directly affecting these outcomes. Biocompatibility assessments indicated no cytotoxic effects, supported by the favorable cellular responses (> 92 % viability compared to control group). These findings underscore the critical impact of MBG particle size on developing advanced CPCs for biomedical applications, guiding future design and optimization strategies.

1. Introduction

While autologous grafting is widely accepted as the golden standard for graft materials, obtaining sufficient amount of bone can be impractical due to the donor site limitations [1]. Consequently, extensive studies have explored calcium phosphate bone cements (CPCs) as an alternative since their discovery in the 1980s [2,3]. Many studies continue to be carried out to advance both the physicochemical and biological properties of CPCs, owning to their self-setting properties, low shear viscosity, biocompatibility, osteoconductivity, and similarity to the bone inorganic phase. Despite the numerous advantages associated with CPCs [4,5], recent research highlighted the need for enhancements in their mechanical and rheological properties. Most often these improvements involve the addition of inorganic compounds like calcium carbonates, calcium sulfates [6,7] and bioactive glasses[8,9] or organic compounds such as polymers [10,11]. However, in the story of CPC improvement, other fundamental aspects such as micro/macro structure, cohesiveness, injectability, setting or physicochemical and mechanical properties for the clinical applications should be carefully considered. As it has been recently summarized in the authors' review paper [12] as well as in studies by Larsson et al. [13] and Coathup et al. [14], adjustments in these properties can be facilitated or impacted by factors including solubility and particle size of the cement powder phase, characteristics of the liquid phase (e.g. pH) and finally the ratio of powder to liquid phase. Solubility of the powder phase is crucial for controlling the rate of cement degradation and bioresorption. The pH of the liquid phase influences the setting time, mechanical properties, and biocompatibility of the resulting cement. Particle size of the powder phase affects the surface area available for reaction and ultimately, the mechanical properties and injectability of the cement. The characteristics of the liquid phase, including viscosity, density, and composition, significantly influence the setting time, workability, and final properties of the cement. Additionally, the ratio of powder to liquid phase determines the consistency, setting time, porosity, and mechanical

* Corresponding author.
E-mail address: dagnija.loca@rtu.lv (D. Loca).

https://doi.org/10.1016/j.matdes.2024.113463
Received 21 June 2024; Received in revised form 11 November 2024; Accepted 12 November 2024
Available online 14 November 2024

strength of the resulting cement, with higher ratios leading to stronger but less flowable cements, and lower ratios improving injectability at the expense of mechanical properties.

CPCs are widely investigated and are already utilized in clinical applications as they achieve general requirements mentioned above. Their main problems are not having the optimal scaffold form for degradation and bone ingrowth. After their setting, a dense cement scaffold shows insufficient porosity and low specific surface area, which results in limited *in vivo* resorption and slow new bone formation rate. In recent years, there has been a notable evolution in the field of CPC manufacturing, with a discernible shift in focus towards enhancing biological responses, as well as their slow degradation and resorption rate *in vivo* [15]. This new paradigm emphasizes fostering intricate interactions between CPCs and cells or tissues, particularly in the context of bone tissue engineering applications [16]. Therefore, incorporating osteopromotive or osteoinductive factors into CPCs is essential to enhance their overall biological performance [17–19]. The simple preparation of CPC offers the flexibility to incorporate sensitive biological components such as proteins, growth factors, and drugs, or to be readily modified by introducing inorganic bone stimulants like ions or bioactive glasses. Bioactive glass-incorporated CPC composites are currently a compelling choice for enhancing the biological performance of implant materials [12]. For instance, bioactive glass 45S5 releases Ca, P, and Si ions, forming a hydroxycarbonate apatite (HCA) layer on its surface similar to mineralized bone. This layer has the potential to bond with host bone, promoting new bone growth [15]. The dissolution products and bioactive surface of BGs significantly influence bone cell activity, by triggering osteoblast expression and supporting the differentiation of osteoblasts from bone marrow stromal cells. Moreover, mesoporous bioactive glass (MBG), a promising type of BG, has been used to overcome the degradation problem of CPC by increasing the porosity over time, which has been followed by the enhanced degradation rate of CPC composite structure [20]. Indeed, MBG offers enhanced surface area (200–500 m^2/g) and pore structure (mesopores with diameters around 5 nm in a very narrow pore size distribution), facilitating improved drug delivery and cell interaction for the applications in the tissue regeneration [20,21].

It has been shown that the incorporation of 45S5 BG into the matrix of calcium tetraphosphate (TTCP) and dicalcium phosphate anhydrous (DCPA)-based CPCs enhanced injectability and compressive strength (up to 40 MPa), while extending the cement setting time from 15 min to 25 min [22]. El-Fiqi et al. [23] explored the integration of MBG nanoparticles (80 nm in size with ~ 5 nm mesopores) into tricalcium phosphate (α-TCP) and calcium carbonate ($CaCO_3$) based CPCs [17]. Addition of MBG nanoparticles to the cements increased the final composite specific surface area from 3.5 m^2/g to 14.2 m^2/g, accelerating its setting reaction from 108 min to 25 min. The compressive strength of MBG nanoparticle-containing cements increased after immersion in simulated body fluid (SBF), from 12 MPa for the pure cement to 26 MPa for the 10 % MBG addition. Moreover, the inclusion of MBG nanoparticles enhanced the injectability of CPCs from 60 % to 75 %, in contrast to traditional CPCs. Similarly, a plethora of studies [22–31], demonstrated diverse improvements in the physicochemical properties of cement structures with BG or MBG additions. These studies encompassed various BG compositions, preparation methods, particle sizes, underscoring the importance of such factors in optimizing cement performance [12].

The rheological properties, such as shear thinning, thixotropy, viscosity and moduli, are closely related to the fluidity and injectability of the bone cements. For instance, smaller particle sizes (up to 100 μm) generally result in lower viscosity and higher fluidity due to increased surface area and reduced particle–particle interactions [32]. This can enhance the injectability of the cement, reducing the likelihood of filter-pressing during extrusion from a syringe. Moreover, the rheological behavior of bone cement, which is influenced by the particle size, affects its ability to flow and fill voids within the bone structures during the application. Wu et al. [32] provided us with an understanding of the relationship between particle size and rheological properties, stating that it is crucial for optimizing bone cement formulations to ensure effective implant fixation and improve clinical outcomes. Building upon the work of Mabroum et al. [33], who studied the effect of different particle size of melt-derived 46S6 BG (coarse BGc: 100–200 μm, medium BGm: 40–100 μm, and fine BGf $<$ 40 μm) on the physicochemical and mechanical properties of CPCs, our research specifically focuses on the setting kinetics, compressive strength, phase transformation and preliminary *in vitro* cellular response of sol–gel derived mesoporous 58S bioactive glass incorporated CPCs, using low temperature synthesized α-TCP as a powder phase for CPC preparation [34]. Sol-gel derived 58S MBG (containing 58 wt% SiO_2, 33 wt% CaO and 9 wt%P_2O_5) have attracted increased attention due to its extensive bone bonding capacity. The sol–gel process helps to improve bioactivity, compared to the melt-derived glasses with same composition, owning to the significantly porous structure of the formed powder [35]. It has been estimated that the concentration of 45–52 wt% SiO_2 is sufficient for bonding both to the bone and the soft tissue, whereas 52–60 wt% SiO_2 allows only bonding to the bone. If the weight concentration of SiO_2 is above 60 wt%, the rate of bone bonding significantly decreases, rendering the material biologically inactive [35]. Moreover, it has been previously proved that sol–gel derived 58S MBG not only facilitate enhanced bioactivity and faster calcium deficient hydroxyapatite (CDHAp) formation (after 8 h, compared to 100 h for other BGs) [36], but also stimulate the gene expression of osteoblastic cells (such as col-I, osteopontin, osteocalcin, BMPs, ALP, osteonectin) [25,37].

Given the limited existing literature on the effects of varying particle sizes and quantities of MBGs in bone cements, our study aimed to validate the hypothesis that controlled incorporation of MBG powder enhances the physicochemical properties of α-TCP-based injectable bone cements. Specifically, we investigated the impact of different 58S MBG particle sizes (the fine particle size $<$ 20 μm, the medium particle size $<$ 38 μm and the coarse particles $<$ 100 μm) and two different weight percentages of 58S MBGs (7 and 9 wt%) on the properties of the final composites. Our research elucidates the critical influence of 58S MBG particle size on the augmentation of octacalcium phosphate forming bone cements. Through systemic experimentation, we sought to preserve the initial crystalline phase of the cement while enhancing its bioactivity and maintaining "ideal" properties of injectable bone cements. This was achieved by assessing setting time, setting reaction, compressive strength, porosity and *in vitro* bioactivity alongside conducting a preliminary cell study. We evaluated these parameters to validate our hypothesis and to advance the understating and development of bioactive injectable bone substitute materials.

2. Materials and methods

2.1. Materials

Chemical reagents, including P123 (Pluronic acid, non-ionic polyethylene glycole (PEG)-polypropylene glycole (PPG)-polyethylene glycole (PEG) block copolymer (Mw = 5800), Hydrochloric acid (HCl), tetraethyl orthosilicate (TEOS), $Ca(NO_3)_2{\cdot}4H_2O$, triethyl phosphate (TEP), calcium nitrate tetrahydrate ($Ca(NO_3)_2{\cdot}4H_2O$), sodium hydroxide (NaOH) were purchased from Sigma Aldrich, USA. Ammonium hydrogen phosphate ($(NH_4)2HPO_4$) were supplied from Merck, Germany. All reagents used to prepare simulated body fluid (SBF), as listed in Kokubo et al. [38] were supplied from Sigma-Aldrich, USA. Phosphate buffer saline (PBS) in tablet form, Dulbecco's modified eagle solution (DMEM) and Dulbecco's phosphate buffered saline (DPBS) were purchased from Sigma Aldrich (Darmstadt, Germany) and Gibco™. Ethanol (EtOH, BioUltra, ≥ 99.8 %, molecular biology grade, CAS: 64–17-5) was purchased from Sigma-Aldrich, USA. 24-well, 6-well plates (Ref. N. 30024) bought from SPL Life Sciences, Korea. Minimum essential medium α (MEM-α), penicillin–streptomycin, fetal bovine serum (FBS) and

Trypsin EDTA 1X were acquired from Gibco™, Thermo Fisher, USA.

2.2. Synthesis of 58S mesoporous bioactive glass

The composition of 58S mesoporous bioactive glass (58S MBG) comprises the 58 wt% SiO_2, 33 wt% CaO and 9 wt% P_2O_5. To prepare the sol, 4.0 g of Pluronic P123 was dissolved in 60 g of 96 % ethanol and left to stir at room temperature (RT). Simultaneously, 1 g of 0.5 M HCI was added while dissolving P123. Once completely dissolved, 6.7 g of TEOS was added and allowed to mix for 30 min at RT. Subsequently, 4.637 g of $Ca(NO_3)_2{\cdot}4H_2O$ and 0.769 g of TEP were added sequentially at an interval of 30 min at RT. The complete sol was stirred at RT for 24 h. The resulting sol was poured into a Petri dish to undergo the evaporation-induced self-assembly (EISA) process for one week. The dried gel was calcined at 700 °C for 5 h, with a heating rate of 2 °C/min, and grinded to obtain the final 58S MBG products. Then the grinded powders were sieved using 20 μm, 38 μm, and 100 μm sieves to obtain the 58S MBG particle sizes as follows: the fine particle size < 20 μm, the medium particle size < 38 μm and the coarse particles < 100 μm. The particle size distribution ($n = 3$ different batch of sieved powder) of sieved 58S MBG particles was determined using the Mastersizer 3000 laser diffraction device with dry dispersion unit Aero S (Malvern Panalytical, The Netherlands). The specific surface area (SSA), pore size and pore volume distribution of synthesized powders were analyzed by using nitrogen adsorption using a Quadrasorb SI (Quantachrome Instruments, USA) and determined by the Brunnauer, Emmet and Teller (BET) method. Prior to analysis, the synthesized powders were degassed for 24 h in the Autosorb Degasser (Quantachrome Instruments, USA), under vacuum conditions at room temperature.

2.3. Synthesis of α-Tri calcium phosphate

α-TCP powder was synthesized with the purity ranging from 98-99 % as described in our previous work [34]. Briefly, amorphous calcium phosphate (ACP) was synthesized via wet precipitation route by dissolving $(NH_4)_2HPO_4$ (21.39 g in 540 mL) and $Ca(NO_3)_2{\cdot}4H_2O$ (57.38 g in 540 mL) in distilled water and adjusting pH of the solution to ~ 10.0, at RT, by using 7 M NaOH. Then these two solutions were simultaneously mixed together, obtained precipitates were filtered, washed and lyophilized (BETA 2–8 LCSplus, Martin Christ Freeze Dryers, Osterode, Germany) for 72 h. Thermal treatment of ACP powder was carried out by heating it at 650 °C for 1 h to obtain α-TCP powder.

2.4. Preparation of 58S-MBG incorporated α-TCP composites (α-TCP/MBG composites)

Each formulation, either without (α–TCP) or with 7 and 9 wt% of 58S MBG (α-TCP/MBG), was prepared by mixing the powder to liquid phases for 30 sec. A solution of 0.5 M $Na_2HPO_4{\cdot}2H_2O$ and 0.5 M $NaH_2PO_4{\cdot}2H_2O$, at pH 6.0, was used as the liquid component for the cement preparation. The optimal powder/liquid (P/L) ratio was determined to be 0.4 g/mL, which was the minimum necessary to obtain a workable paste. Experimental groups are given in the Table 1. Additionally, composite containing different 58S MBG particle sizes were prepared. The sample groups were labelled based on the amount of 58S MBG added and its particle size based on the sieving mesh size used.

The cement composite pastes were placed into the Teflon molds (5 mm in height and 10 mm in diameter) and stored at 37 °C at desired time intervals for further analysis.

Table 1
Composition of cement, liquid component, percentage of 58S MBG, P/L ratio.

Median Particle Size of MBG	Abbreviation	MBG (wt%)	Liquid phase	P/L ratio (g/mL)
–	BG0	–		
10.9 μm	BG7-20			
37.8 μm	BG7-38	7	0.5 M $Na_2HPO_4{\cdot}2H_2O$ and	
66.3 μm	BG7-100		0.5 M $NaH_2PO_4{\cdot}2H_2O$	0.4
10.9 μm	BG9-20		mixture at pH 6.0	
37.8 μm	BG9-38	9		
66.3 μm	BG9-100			

2.5. Setting time measurement

The setting time of prepared cements was measured according to the Gillmore needle method, based on the international standard ISO 9917, at RT. Gillmore apparatus has two needles and measures the initial-setting time with a needle having 113.4 g weight and 2.12 mm diameter and the final setting time with a needle having 453.6 g weight and 1.06 mm diameter. The initial and final setting times were considered as the time in which the paste hardened to such an extent that needle would not penetrate deeper than 1 mm into the prepared composites. Three replicate specimens were tested for obtaining the average setting time values.

2.6. Compressive strength measurements

α-TCP/MBG composites were placed into cylindrical Teflon molds with a diameter of 10 mm and a height of 20 mm. The cement composites were allowed to stay in a mold until they set. Subsequently, the compressive strength of α-TCP/MBG composite specimens (5 replicates for each group) was measured at a loading rate of 1 mm/min, using a screw-driven Instron universal testing machine (Norwood, MA, USA), with a 30000 N load cell.

2.7. X-ray diffraction (XRD) analysis

X-ray diffraction (XRD, Miniflex 600 HR, Rigaku, Japan) analysis of synthesized powders and 58S MBG incorporated α-TCP composites was performed. Prior to XRD measurements, the powders were dispersed on the low background silicon wafer. The XRD measurements were performed with 40 kV and 15 mA, in the range of 3–70° 2Θ, with a step size of 0.0330 ° and a scan step time (s) of 51.1651. The XRD patterns were then discerned by HighScore software (Malvern Panalytical, United Kingdom), and compared with the reference patterns from the International Centre for Diffraction Data (ICDD®) database. Following ICDD entries were used for the crystalline phase identification: 26–1056 for octacalcium phosphate (OCP), 009–0348 for α-TCP and 0–009-0432 for CDHAp.

2.8. Scanning electron microscopy (SEM) and scanning transmission electron microscopy (STEM) measurements

Synthesized powders and cross-sectional morphology of MBG incorporated samples after 24 h incubation at 37 °C were observed by using SEM (SEM Auriga, Carl-Zeiss, and Jena, Germany). Sample image generation was performed with a combination of secondary electrons and back-scattered electrons, created at an acceleration voltage of 5 kV. The elemental composition of the synthesized 58S MBG powder was analyzed using energy dispersive X-ray spectroscopy (EDX detector Oxford X-Max 150, UK) to identify the presence of Ca, P and Si elements. To assess the mesopore formation of synthesized 58S MBG powders, scanning transmission electron microscopy (STEM, Thermofisher PV3-137, USA) was employed. Prior to STEM analysis, powders were prepared by ultrasonication in isopropanol for 5 min to form homogeneous suspensions. Mesoporous structures were then imaged using STEM at 30 kV accelerating voltage. SEM was also applied to evaluate the cross-sectional microstructure of the formulated cements after setting, using Field emission-SEM (FE-SEM) (Tescan Mira/LMU, Czech Republic) at an acceleration voltage of 15–25 kV and a distance of 8–10 mm. Similarly, cross-sectional microstructure of the formulated cements after 21 days

of incubation in SBF was examined by using SEM (Thermofisher PV3-137, USA) at an acceleration voltage of 15–25 kV and a distance of 8–10 mm. All the specimens were attached to the aluminum stubs by using double-sided adhesive carbon tape and coated with a thin conductive layer of gold using a sputter coater (Emitech K550X, Quorum Technologies, Ashford, Kent, and United Kingdom).

2.9. Porosity and specific surface area measurements

The open (P_o), closed (P_c) and total (P_t) porosity of α-TCP/MBG composites were determined by the Archimedes method, as described in our previous work and in the literature [34,39]. The following equations were used to calculate the porosity % of the samples:

$P_o = (m_1\text{-}m_0)/(m_1\text{-}m_2)*100.$

$\rho_{Ap} = m_0/(m_1\text{-}m_2).$

$P_t = 100\text{-}((\rho_{Ap}*100)/\rho_{Th})).$

$P_c = P_t\text{-}P_o.$

where m_1 — weight of impregnated sample, m_0 — weight of dry sample, m_2 — weight of impregnated sample in the water, ρ_{Ap}— apparent density of the sample, ρ—t heoretical density of the sample determined by using pycnometer (ULTRAPYC 1200e), and P_c — closed porosity of the sample. Three replicates of samples were used.

The Quadrasorb™ SI Surface Area and Pore Size Analyzer (Quantachrome Instruments, USA) was employed to produce nitrogen adsorption–desorption isotherms for the α-TCP/MBG composites at a temperature of −196 °C. Prior to analysis, the α-TCP/MBG composites were degassed for 24 h in the Autosorb Degasser (Quantachrome Instruments, USA), under vacuum conditions at RT. The Brunauer–Emmett–Teller (BET) model was utilized to calculate the specific surface area (SSA) of the prepared composites based on their adsorption isotherms within the pressure range of 0.05 to 0.3P/P0.

2.10. Bioactivity and ion release measurements

After setting, the cement samples were placed into SBF at 37 °C for 1, 7, 14 and 21 days. SBF solution was prepared by using the method described in Kokubo et. al. [38]. Bioactivity and crystallization of the samples were examined by using XRD (Miniflex 600 HR, Rigaku, Japan) as described in the section 2.6. Three replicate samples were used for each time point. To examine the formation of apatite during the incubation period of the composites, phase composition were analyzed using Profex software (version 5.1, Solothurn, Switzerland) [40]. Additionally, SEM analysis was performed to observe morphological changes on the surface of the cement composite after the SBF incubation.

The pH of the SBF solution was also monitored during the incubation period, with additional time points including 1 and 6 h of incubation. Composite samples (n = 3 per group) were dried and their wright change % were calculated by using the following equation:

$$\frac{\textit{initial dry weight} - \textit{dry weight after incubation}}{\textit{initial dry weight}} \times 100\%$$

To analyze ion exchange between the cement composites and the cell medium, Ca, P, and Si ion concentrations were quantified using an inductively coupled plasma mass spectrometer (ICPMS, Agilent Technologies 8900, CA, United States). Hardened cement composites were submerged in α-minimal essential medium (α-MEM, Gibco, USA) supplemented with 10 % FBS (Gibco, USA) and 1 % penicillin–streptomycin (Gibco, USA), maintaining a weight/volume ratio 0.1 g/mL. The samples were then incubated in shaking incubator at 37 °C. At specified time intervals starting from day 1, aliquots were taken out and released amount of ions was analysed. 4 mL medium was removed after each time point (1,3, 7, 14 and 21 days) and replaced with 4 ml of fresh medium. The collected liquid samples were then acidified with trace grade nitric acid (0.5 mL HNO_3,) and hydrofluoric acid (0.05 mL HF, Fischer Scientific, Trace grade) to a total volume of 50 mL per sample. Samples were diluted as necessary to comply with the calibration range and analyzed for chemical elements using ICP-MS equipped with a Micromist nebulizer and a He collision/reaction cell. The calibration of the equipment was performed using ICP-MS standard stock solutions traceable to NIST SRM – Ca, PO_4 standard solutions (Merck, 1000 mg/L), and Multielement Standard Solution 6 for ICP (Sigma Aldrich, 100 mg/L). An external calibration graph with blank correction was employed, with deionized water as the blank solution. The calibration graph was constructed using a concentration range of 0.1 μg/L to 100 μg/L for Si and 1 mg/L to 10 mg/L for Ca and PO_4. To ensure system stability control, a 10 μg/L internal standard mix solution of Bi, Ge, In, Sc, Tb, Y, and Li was used. After every ten samples, one standard solution was introduced into the system to verify the stability of measurements. The measurements were made in the MS/MS configuration using He as the collision gas and O_2 as the reaction gas. The same ICP-MS methodology was applied to measure the Ca/P ratios of hardened cement samples after setting and after immersion in simulated body fluid (SBF) for 21 days. For this part of the measurement, samples were prepared using a microwave-assisted digestion method. A mixture of 8 mL of nitric acid (HNO_3, Fisher Scientific, Trace Grade) and 0.2 mL of hydrofluoric acid (HF, Fisher Scientific, Trace Grade) was added to 0.2 g of each sample. This mixture was then heated in a Milestone Start E microwave furnace for 30 min at 180 °C. After the digestion process was completed, each sample was diluted to a total volume of 50 mL with deionized water (Grade 1, electrical conductivity < 0.055 μS/cm).

2.11. Indirect cell viability measurements

The pre-osteoblasts, MC3T3-E1 cell line (ATCC, USA), were used for cytocompatibility test. Cytocompatibility tests were performed via the indirect method, according to the guidelines of ISO10993-5. Before the cell seeding, cement samples (3 replicates for each group) were sterilized by using 70 % ethanol (30 min) and UV light (30 min for each side of the samples), then they were placed in 50 mL falcon tubes and immersed in a cell culture medium (supplemented with 10 % FBS (Gibco, USA) and 1 % penicillin–streptomycin (Gibco, USA), with 0.1 $g{\cdot}mL^{-1}$ sample/medium ratio and incubated at 37 °C with a gentle shaking (75 rpm). The extracted cell culture medium was collected after 1, 3, 7 and 21 days.

Cells were plated in α-minimal essential medium (α-MEM, Gibco, USA) supplemented with 10 % FBS (Gibco, USA) and 1 % penicillin–streptomycin (Gibco, USA). When cells were confluent, 1×10^4 cells/well were cultured in a 96-well plate. Cells were allowed to attach on the bottom of the well-plate for 24 h. After 24 h, cell culture medium was replaced with extracted medium of each day (day 1, 3, 7 and 21 days of extracts; with 3 replicates for each extracted medium). Cells were treated with this medium for additional 24 h. A cell-seeded tissue culture plate was used as a positive control, while cell treated with a medium containing 10 % DMSO medium served as a negative control. The *in vitro* cytocompatibility was assessed using the cell metabolic activity measurement (CCK-8 assay), fluorescent staining, and microscopic analysis of cell morphology.

2.12. Statistical analysis

Results were given as a mean value ± standard deviation; the number of replicate samples used for each test is indicated in the Figure captions as well as in method description. Differences between the groups were analyzed by using GraphPad Prism (Version 9.2.0., GraphPad Software, USA).

3. Results and discussion

3.1. Characterization of the synthesized powders

Fig. 1 (A) shows the XRD diffraction patterns of the prepared 58S MBG and α-TCP powders. The XRD diffractograms of 58S MBG only shows the broad peak between 18 and 30° (2θ) typical of amorphous glass-like materials. The broad amorphous diffraction peak at approximately 23° is typical for Si-based glasses, whereas the broader peak at around 30° may indicate the presence of amorphous calcium silicates or calcium phosphates[41]. No crystalline structures were found. Similarly, nanocrystalline α-TCP diffractogram matches the crystalline structure pattern of the reference α-TCP (ICDD: 00–009-0348).

The particle size distribution of 58S MBG powders with three different sizes were calculated by using SEM images of the samples on Image J software and given in Fig. 1(F). Additionally, particle size distribution results measured by using laser diffraction device with dry dispersion unit is given in Fig. 1 (G). The mean particle sizes for sample groups, labeled according to the sieving mesh sizes of 20, 38 and 100 μm, are 12.10 ± 0.75 μm, 19.30 ± 5.06 μm and 51.74 ± 25.33 μm, respectively. In addition, the median particle size for sample groups was obtained as 10.9 μm, 37.8 μm and 66.3 μm, respectively.

Supplementary Figure (SF) 1 shows N_2 adsorption–desorption isotherm of the 58S MBG and α-TCP powders. The isotherms displayed a distinct hysteresis loop for MBG powders, indicating the presence of mesoporous structures within powder. This mesoporosity likely contributed to the capillary condensation observed in each sample, consistent with the formation of a hysteresis loop. As shown in Table 2, the average BET surface area of the 58S MBG powder was approximately 171.86 m^2/g, with a pore size of 12.15 nm, which falls within the mesoporous range (2–50 nm) according to the International Union of Pure and Applied Chemistry (IUPAC) classification [42]. The total pore volume of the MBG powders was also relatively high (0.49 cm^3/g), which could facilitate greater interactions in composite applications. In contrast, the α-TCP powder exhibited a much lower BET surface area of 11.32 m^2/g and a total pore volume of 0.02 cm^3/g, indicating limited mesoporosity compared to the MBG powders.

Table 2
Average pore size, Brunauer-Emmett-Teller (BET) surface area, and total pore volume of α-TCP and 58S MBG powders.

Samples	α-TCP	58S MBG
Average pore size (nm)	9.73 ± 1.16	12.15 ± 4.53
BET surface area (m^2/g)	11.32 ± 0.39	171.86 ± 44.34
Total pore volume (cm^3/g)	0.02 ± 0.00	0.49 ± 0.07

STEM was used to examine the nanoscale mesoporous structure of synthesized 58S MBG powder as indicated in Fig. 2 (A). MBGs formed their structure through the hydrolysis and condensation of an alkoxysilane precursor, like TEOS as used here, with a micelle-forming polymer surfactant (P123 here) and calcium/phosphorous-containing reagents. Controlled evaporation of the solvent increases reactant concentration, leading to inorganic-surfactant micelle network formation through EISA. After thermal removal of the polymer surfactant, a highly ordered mesopore network emerges. However, stoichiometric limitations may arise due to variations in precursor quantity and ratio during EISA. In general, pore characteristics remain consistent across varying

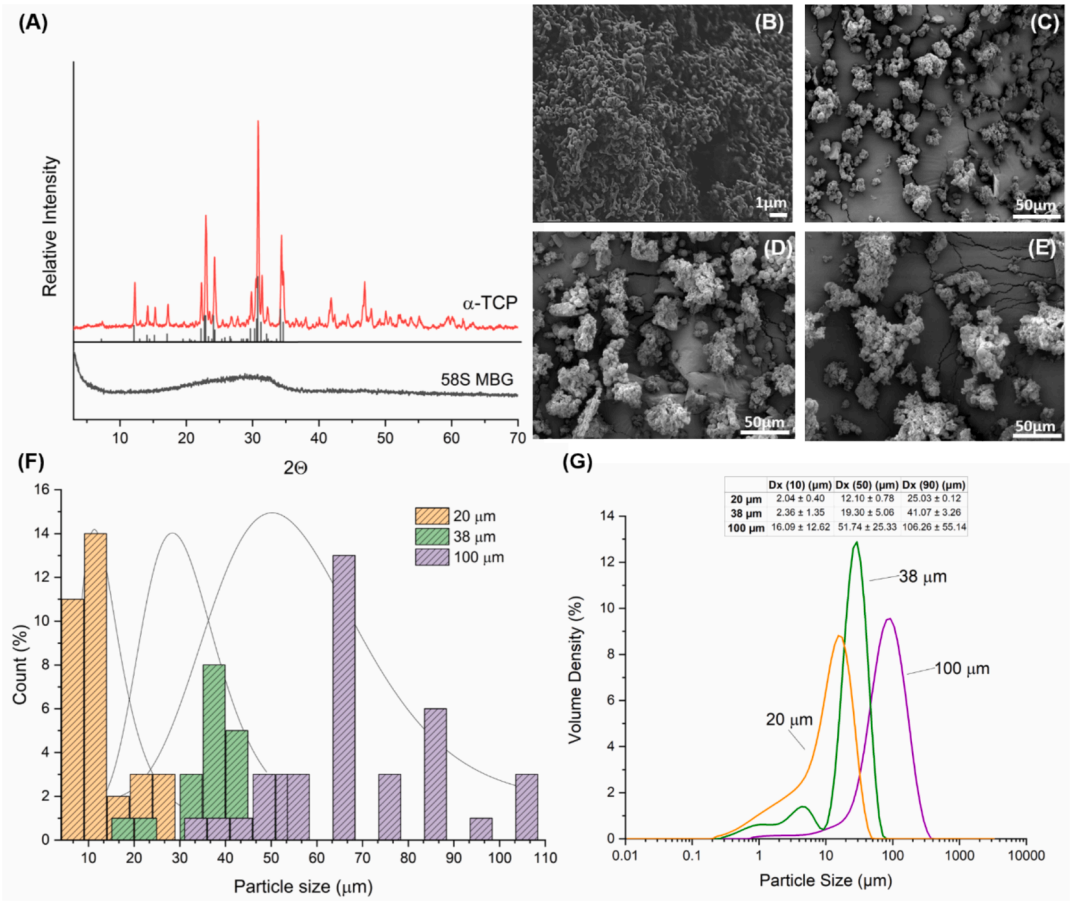

Fig. 1. (A) XRD diffractograms of synthesized α-TCP, reference peaks of α-TCP (ICDD number 00–009-0348), and 58S MBG powders. SEM micrographs of (B) α-TCP powder and 58S MBG powders with median particle sizes of (C) 10.9 μm, (D) 37.8 μm, and (E) 66.3 μm. (F) Particle size distribution of 58S MBG powder calculated from SEM images using Image J software, and (G) measured by laser granulometry.

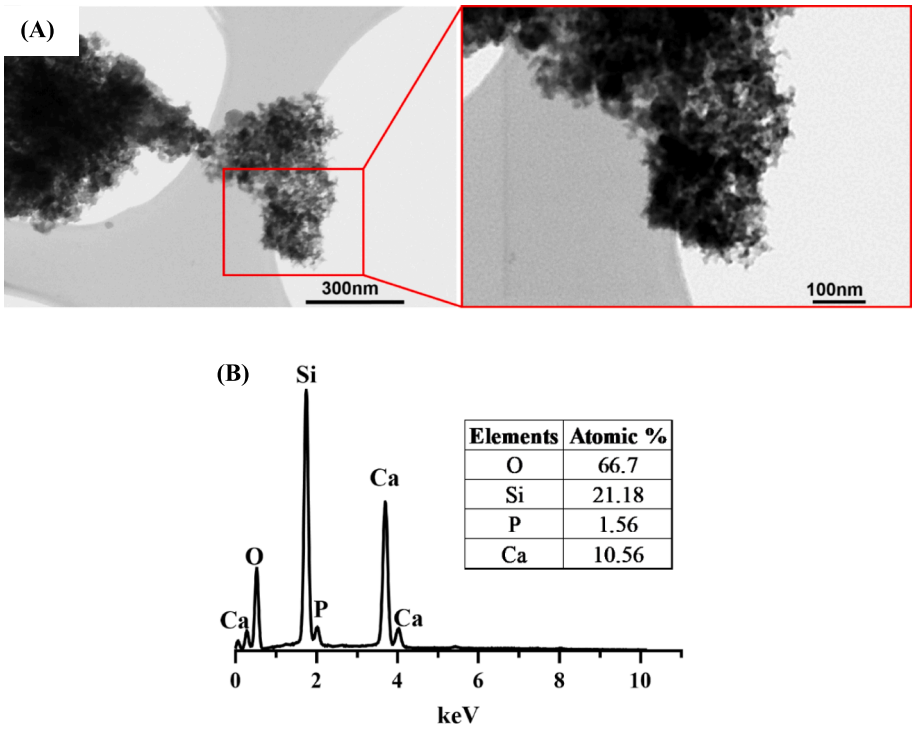

Fig. 2. (A) Representative STEM micrographs of the synthesized 58S MBG powder. (B) EDS spectra together with atomic percentages of each element for 58S MBG powder.

glass stoichiometry under constant process conditions [41]. Representative STEM micrographs revealed that synthesized 58S MBG lacked structured and ordered porosity. Although literature examples demonstrate regular pore network with 58 mol % of SiO_2 content, different surfactant-to-precursor ratio render direct comparisons inappropriate [41,43]. Despite observed differences, significant porosity was evident in STEM micrographs as well as the BET analysis findings. EDS analysis of synthesized 58S MBG powder revealed the primary elements – silicon, calcium, phosphorous, and oxygen – in proportions consistent with 58S bioactive glass composition (Fig. 2 (B). The atomic percentages observed align closely with theoretical calculations for 58S bioactive glass, supporting the effectiveness of the synthesis process.

3.2. Physicochemical and in vitro characterization of the α −TCP/MBG composites

3.2.1. XRD analysis

In our previous work, α-TCP powder was used as a sole precursor to produce injectable OCP-forming bone cements due to its ability to react with water and set at room temperature [34]. Without the addition of BG as a secondary powder phase, our cements formed an OCP phase after setting (labelled as BG0). OCP has been widely recognized for its potential in bone tissue regeneration, owing to its pivotal role as a precursor phase for apatite formation. Its distinctive feature lies in its swift transformation into the apatite form upon implantation, adding another dimension to its utility [44]. The transformation of the OCP phase into apatite increases the likelihood of incorporating impurities like carbonate or magnesium ions from the surrounding environment into the apatite structure. This process mimics the non-stoichiometry found in natural bone apatite. Building on our previous research highlighting the significant role of pH in OCP formation after setting, we sought to investigate the impact of BG addition on this process. The phase conversion process of the α-TCP/MBG composites was discussed regarding the MBG particle size and added weight percentage amount.

To assess the phase conversion dynamics of our prepared composites both post-setting and over time, we immersed the samples in SBF at 37 °C for up to 21 days. Subsequently, we stopped the reaction at each time point by submerging the samples in acetone for 15 min before analyzing them. The XRD patterns of our α-TCP/MBG composites, illustrated in Fig. 3 and spanning the 3–70° 2θ range, unveiled intriguing insights. Notably, the cements BG0, BG7-100, BG7-38 and BG9-100 revealed that the characteristic peak of OCP phase at 4.72° 2θ was visible in the patterns after setting and after 1-day incubation in SBF. Additionally, results revealed that incorporation of MBG into α-TCP cements interfered with the formation of OCP phase while promoting the apatite formation. As evidenced by Fig. 4, the presence and phase percentage of OCP increased with the particle size of MBG; suggesting a faster reaction with larger MBG particle sizes [33].

After 1st day, apatite phase became more pronounced for MBG incorporated samples than for the BG0 sample, as seen in the range of 10° – 40° 2θ. The characteristic peaks of the OCP phase at 4.72° disappeared from the XRD diffractograms (Fig. 3 (C)) of BG7-100, BG7-38 and BG9-100 after 7 days of incubation in SBF. Interestingly, the BG7-38 sample showed the presence of the OCP phase after setting and after 1 day of SBF incubation whereas the BG9-38 sample did not. This is clearly reflected in the increase in apatite % and the corresponding decrease in OCP phase %, as shown in Fig. 4. Furthermore, the XRD patterns of α-TCP/MBG composites also demonstrated phase transformation after 7 days of incubation in SBF, showing the presence of apatite peaks with varying intensity and phase percentage, depending on the size and quantity of MBG powder. The differences in percentages can be attributed to variations in ion supersaturation, with MBG inclusion and smaller particle sizes exhibiting higher apatite percentages, while samples without MBG and larger particle sizes displayed the lowest apatite percentages. These findings suggest that while the apatite formation reaction generally accelerated with higher MBG weight percentages and smaller particle sizes, other factors such as the specific weight percentage and distribution of MBG particles also play a significant role in the phase transformation dynamics. Moreover, the conversion of OCP to apatite reflects the non-stoichiometry seen in natural apatite, with this

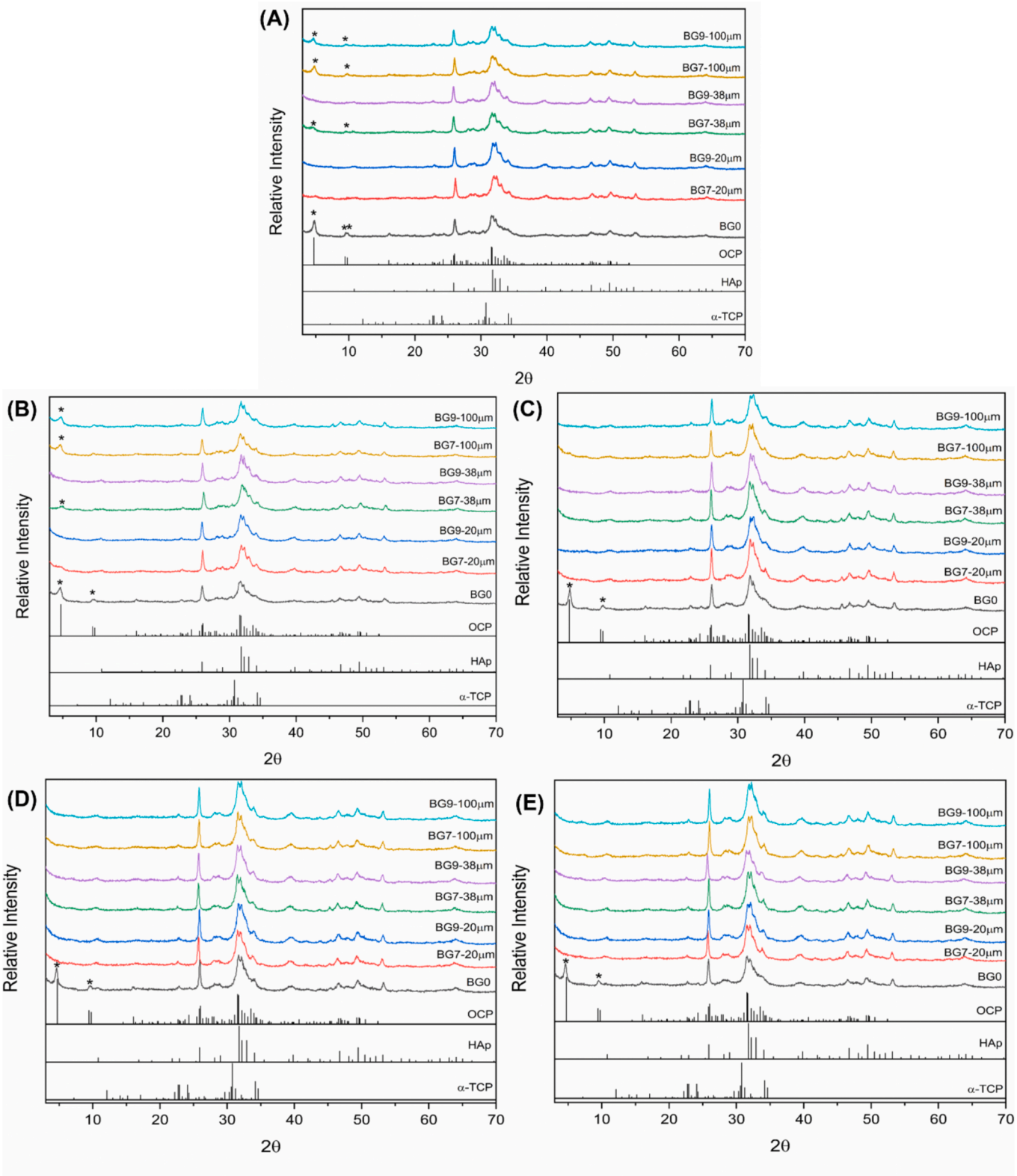

Fig. 3. XRD patterns of α-TCP/BG composites after setting (A) and incubating in SBF at 37°C for 1 (B), 7 (C), 14 (D) and 21 (E) days. (* characteristic peaks for OCP).

transformation being thermodynamically favored and proceeding spontaneously and irreversibly under physiological pH and temperature [45].

3.3. Setting time measurements

The setting time of α-TCP and α-TCP/MBG composites is a crucial indicator of their usability and effectiveness in clinical applications, reported to be approximately 15 min [46]. Consequently, we conducted preliminary experiments to formulate our α-TCP/MBG composites.

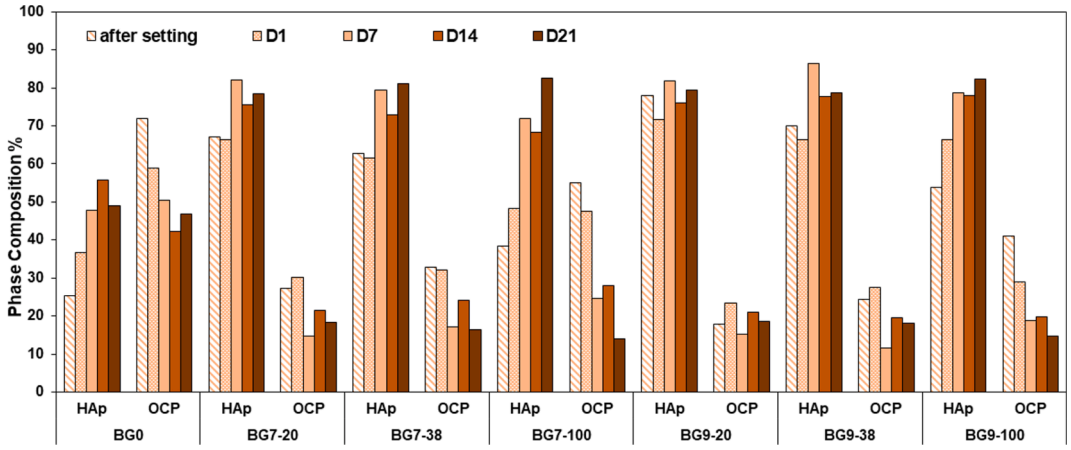

Fig. 4. Phase composition % obtained from the XRD patterns analyzed by using Profex software[40]; showing how OCP and HAp phases are changing during the incubation period of samples in SBF at 37°C.

Notably, when employing a 10 wt% MBG alongside a liquid phase having a pH of 6.0, the α-TCP/MBG composites failed to undergo a setting reaction. Our initial findings on setting time (data not presented) indicated that MBG content of 7 wt% and 9 wt% exhibited promising setting time and were worth exploring the influence of varying particle sizes on α-TCP/MBG composites. Table 3 and Fig. 5 summarize the setting times obtained for each sample, shedding the light on the influence of MBG particle size on the final setting time. The analysis of acquired data revealed a significant correlation between the particle size of 58S MBG and the setting time of α-TCP/MBG composites. As MBG particle size increased, the final setting time decreased by more than 10-fold, when comparing BG9-20 to BG9-100 (see Table 3).

The increase in setting time with decreasing MBG particle size was likely due to enhanced interaction between MBG and α-TCP, resulting in a more homogeneous mixture that took longer to set. The presence of bioactive glass introduced Si ions into the liquid phase, potentially altering the ionic balance and affecting the nucleation and growth of calcium phosphate phases like HAp and OCP. This ionic influence from the MBG particles could contribute to the observed delay in setting time. This mechanism aligns with findings from Mabroum et al. [33], where they observed a similar setting delay when bioactive glass particles were used. In their study, they used 46S6 BG powder with fine (≤40 μm), medium (40–100 μm), and coarse (100–200 μm) particle sizes. The final setting time of their cement with these BG-added samples was found to be around 134 min, 91 min, and 71 min, respectively. Their initial setting time was also higher than 50 min, which could be attributed to differences in cement formulation and the type of BG used. This underscores the need for precise control of particle size and MBG content in cement formulation.

3.4. Compressive strength and porosity measurements

In this study, compressive strength measurements of α-TCP/MBG composites were conducted immediately after the specific setting time for each formulation. This approach allows for the evaluation of the initial mechanical properties, which are crucial for understanding the cement's performance right after setting in potential clinical applications. Mechanical performance of α-TCP/MBG composites is given in the Fig. 6 (A). While the addition of 7 wt% of MBG into α-TCP cements did not significantly change the compressive strength, the 9 wt% of MBG incorporated showed significant decrease in compressive strength values. Obtained results also revealed that reducing the MBG particle size from < 38 μm to < 20 μm considerably increased the compressive strength of the composites. In contrast, the different trend was observed for the composites with < 100 μm MBG particles. The observed decrease in compressive strength with higher MBG weight percentages can be attributed to the diminished cohesion of the cement paste, evidenced also by the significantly prolonged setting times. The correlation between cross-sectional morphology and compressive strength measurements further supports this explanation.

The addition of smaller MBG particles into α-TCP cement resulted in a more compact structure (Fig. 7), contributing to the higher compressive strength. Conversely, increasing the particle size of MBG led to a higher total porosity of the cement matrix and a decrease in the specific surface area (SSA), thereby explaining the decrease in compressive strength with larger MBG particles. Specifically, incorporation of < 20 μm MBG particles notably increased SSA compared to < 38 μm and < 100 μm particles. This enhanced SSA facilitates greater surface

Table 3
Setting time of cement compositions.

Median Particle size of BG	Abbreviation	Initial Setting Time (min)	Final Setting Time (min)
–	**BG0**	2.9 ± 0.2	6.5 ± 0.4
10.9 μm	**BG7-20**	4.9 ± 0.1	38.2 ± 0.1
	BG9-20	7.1 ± 0.1	115.4 ± 0.1
37.8 μm	**BG7-38**	2.8 ± 0.1	11.6 ± 0.1
	BG9-38	3.4 ± 0.1	16.9 ± 0.1
66.3 μm	**BG7-100**	2.5 ± 0.1	7.9 ± 0.1
	BG9-100	2.7 ± 0.1	10.2 ± 0.1

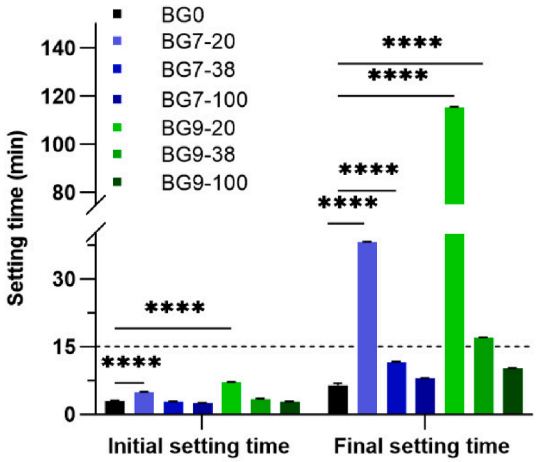

Fig. 5. Initial and final setting time of the α-TCP/MBG composites (3 replicates were used for each group).

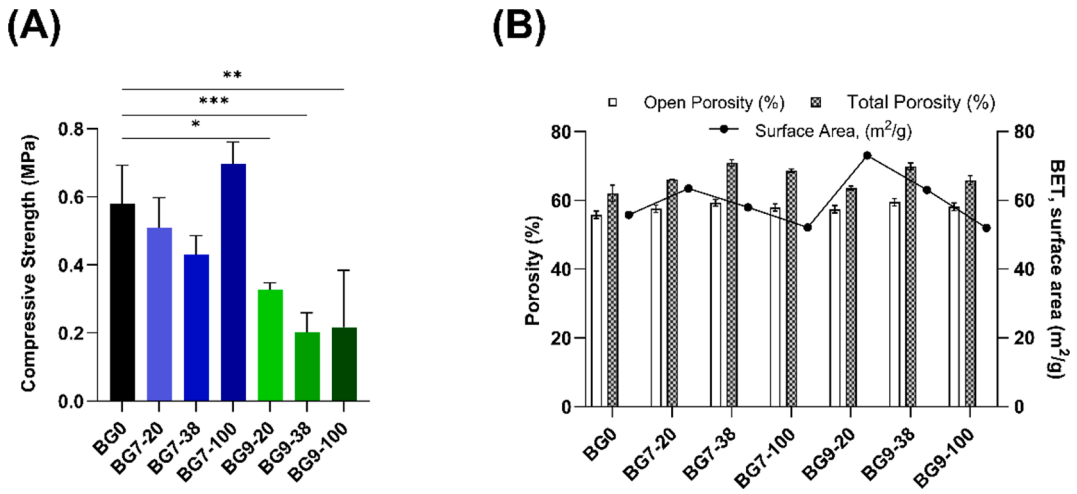

Fig. 6. (A) Compressive strength of cement composites after setting. Date is given as mean ± standard deviations (5 replicates were used in each group), asterisk indicates that BG0 compressive strength was significantly different than that of other composites. (*<0.05, **<0.01 and ***<0.001). (B) Porosity and surface area results of composite after setting (3 replicates were used in each group).

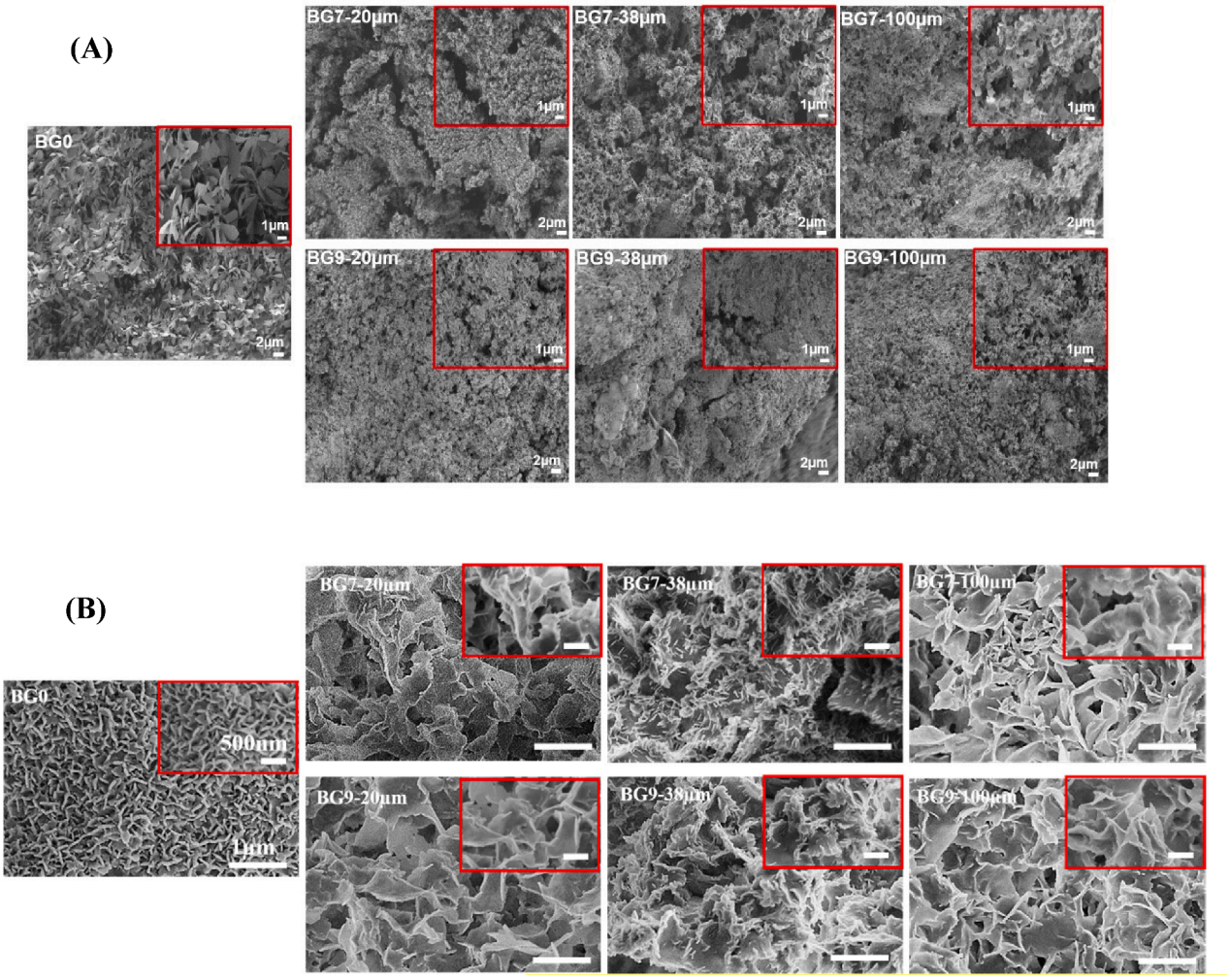

Fig. 7. (A) Cross-sectional SEM images of samples after setting. (B) Cross-sectional SEM images of samples after 21 days of incubation in simulated body fluid (SBF) at 37oC, showing any potential surface or structural changes due to incubation.

interactions and ion release, promoting accelerated apatite formation kinetics within the cement matrix. Consequently, α-TCP/MBG composites containing < 20 μm MBG (BG-20) exhibit faster apatite formation compared to those with larger MBG particles, as presented in subsection 3.2.2. Therefore, optimization of MBG particle size, particularly in the range of around 20 μm, enhances the SSA and accelerates apatite

formation in CPC composites, suggesting improved potential for bone regeneration applications. This interplay between particle size and cement cohesion, as well as the impact on the structural compactness, total porosity and SSA, highlights the intricate relationship affecting the compressive strength of the composite materials.

3.5. Evaluation of cement morphology

The cross-sectional morphology of MBG incorporated α-TCP samples after the setting, as presented in Fig. 7 (A), revealed distinctive microstructural changes compared to the control sample (BG0). The microstructure of BG0 exhibited a plate-like morphology, which could be attributed to the presence of OCP. In contrast, with the incorporation of MBG particles smaller than 20 μm, a denser and more compact microstructure was observed, characterized by the presence of fine, needle-like crystals indicative of hydroxyapatite formation. These needle-like crystals suggested that MBG addition enhanced the formation of hydroxyapatite within the cement matrix, promoting a more homogeneous and compact structure compared to the OCP-dominated BG0 sample. This observation is in line with the work of Ginebra et al. [47], who demonstrated that the incorporation of smaller particle sizes leads to the formation of smaller apatite crystals in α-TCP-based cement. Thus, our findings not only corroborate existing literature, but also provide insight into the role of MBG in influencing the microstructural properties of α-TCP based cement, by resulting in dense/compact microstructure. Following 21 days of incubation in simulated body fluid (SBF) at 37 °C (Fig. 7 (B)), further morphological transformations were apparent across all MBG-incorporated samples, indicating phase conversion and mineral deposition. These structural changes, particularly the increased surface roughness and porosity, aligned with the Ca/P ratio results (Table 4), which showed an increase in the Ca/P ratio for all samples over time. This increase suggested a shift from the initial OCP phase towards apatite, as supported by both SEM morphology and XRD phase analysis (Fig. 3). The formation of OCP in MBG-incorporated cements was expected, given that OCP nucleation under biomimetic conditions was typically faster than HAp nucleation, despite HAp being the thermodynamically more stable phase [48]. The high local ion concentrations created by the MBG particles promote OCP nucleation on the cement surfaces, particularly during the initial setting and early incubation stages. Consequently, the initial appearance of OCP, as confirmed by XRD, was a natural precursor phase that eventually transforms into apatite over time, facilitated by prolonged SBF exposure. The Ca/P ratio analysis (Table 4) provided quantitative insight into the phase transformation dynamics of the cements. Initially, all samples displayed Ca/P ratios below the stoichiometric value for HAp (1.67), indicating the presence of non-stoichiometric [49], Ca-deficient phases like OCP (see Figs. 3 and 4). After 21 days in SBF, the Ca/P ratios of MBG-containing samples increased significantly, reaching values up to 1.33 for BG9-20 and BG9-100. This progression suggests an accelerated transformation towards apatite, facilitated by the MBG particles' rapid ion release, which creates a supersaturated local environment conducive to apatite formation.

Table 4
ICP-MS quantification results for the Ca/P ratio of cement samples after setting and following 21 days of incubation in simulated body fluid (SBF).

Abbreviation	Ca/P ratio After setting	Ca/P ratio After 21 days
BG0	**1.20**	**1.27**
BG7-20	**1.21**	**1.31**
BG7-38	**1.22**	**1.29**
BG7-100	**1.22**	**1.29**
BG9-20	**1.21**	**1.33**
BG9-38	**1.23**	**1.31**
BG9-100	**1.27**	**1.33**

3.6. Acellular bioactivity assessment

The acellular bioactivity assessment of α-TCP/MBG composites is presented in Fig. 8. The pH variation and weight loss were evaluated in SBF at 37 °C under gentle shaking, while ion release was examined in cell culture medium supplemented with 10 % FBS and 1 % pen-strep at 37 °C under gentle shaking. The initial pH increase, followed by stabilization around 6.8 by day 21, indicated rapid ionic exchange and partial dissolution, consistent with the phase transformations observed in XRD analysis. The dissolution of α-TCP and the release of calcium and phosphate ions into the medium created a calcium-rich environment contributing to HAp formation, as confirmed by the appearance of HA-related peaks in XRD over time. The gradual pH drop afterwards was attributed to the properties of 58S MBG, a phosphate-based bioactive glass, which is known to lower pH in solution over time. Studies on similar phosphate-based glasses showed that they tend to decrease the pH of the surrounding environment as they dissolve due to the release of acidic byproducts from the glass matrix [50]. The release of bioactive ions, specifically calcium, phosphate, and silicon, was further supported by SEM observations, which showed progressive mineral deposition on the composite surface. MBG's porous structure enhanced ion exchange, facilitating a sustained release. Notably, 9 wt% MBG samples (BG9) exhibited a higher pH than 7 wt% samples (BG7), indicating that higher MBG content accelerates ion release. No distinct pattern was observed for particle size impact on pH variation, suggesting that MBG content primarily influences dissolution behavior.

The weight loss data illustrated progressive degradation across all samples, with the highest weight loss in BG7-38 and BG9-38, retaining around 87 % and 91 % of initial weight, respectively. Intermediate-sized MBG particles (38 μm) appeared to facilitate greater interaction with the medium, resulting in more substantial degradation, while smaller (20 μm) and larger (100 μm) particles showed slower degradation rates. The control group, BG0, which lacked MBG, exhibited minimal weight loss (~97 %), highlighting MBG's role in promoting degradation through ion release.

The calcium, phosphorus, and silicon ion release data reveal that both MBG content and particle size significantly impacted ion availability over time. Across all samples, ion concentrations increased steadily, with BG9-38 (9 wt% MBG, 38 μm particle size) consistently demonstrating the highest cumulative release of Ca (80.4 μg/mL), P (705.4 μg/mL), and Si (130.4 μg/mL) by day 21. This suggested that the intermediate particle size of 38 μm, combined with higher MBG content (9 wt%), provided conditions favorable for ion release in the tested environment. In contrast, samples with larger particles (e.g., BG9-100) or lower MBG content showed slower ion release, possibly due to differences in the interaction dynamics with the surrounding medium. These results indicated that MBG particle size and content could be adjusted to influence the ion release profile, enhancing the bioactivity of composites for bone tissue engineering.

3.7. Indirect cell culture studies

Fig. 9 shows cell viability and proliferation, as indicated by means of CCK-8 assay and fluorescence imaging analysis. Preliminary cell viability assessment was carried out by using the indirect cell culture method. The ion release of α-TCP/MBG composites was investigated (Fig. 8 (C), (D), (E)), and we observed steady ionic dissolution and precipitation during the cement setting reaction and phase formation process. This study allows us to explore the mechanisms governing the interaction between the ionic dissolution products of bioactive composites and cellular responses. The ion release study provides valuable insights, showing a gradual increase in Ca, P and Si ion concentrations over time. Notably, the Ca concentration in the composite extracts remained below the baseline Ca level in the cell culture medium, suggesting limited additional Ca release from the composites. This limited Ca availability could impact cell signaling processes related to

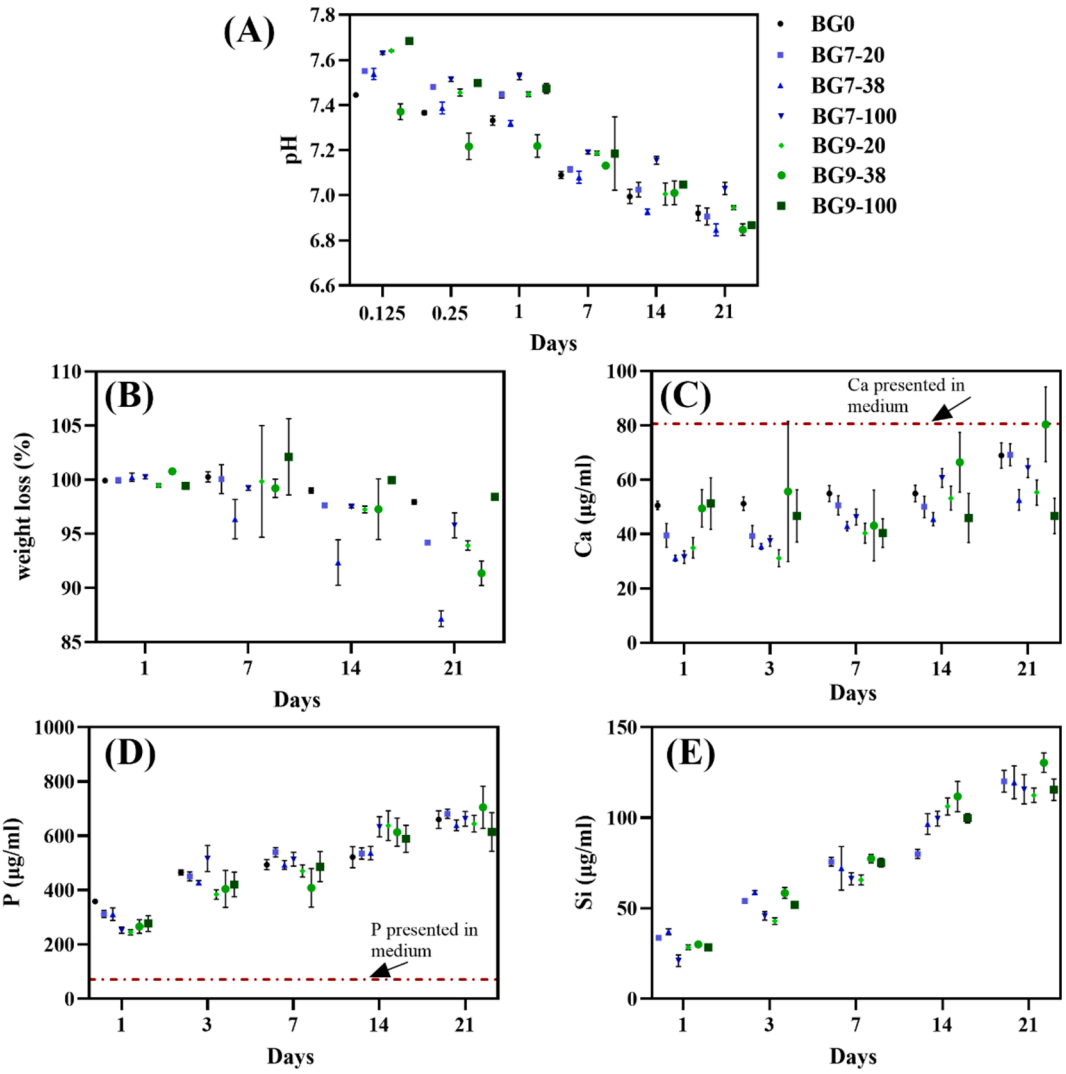

Fig. 8. Acellular bioactivity assessment of α-TCP/MBG composites. (A) pH variation over time, indicating changes in ionic exchange and material dissolution. (B) Weight loss percentage, illustrating the degradation behavior of each composite (initial weight set to 100%). (C) Cumulative calcium ion release, with reference to the baseline Ca concentration in the cell culture medium. (D) Cumulative phosphorus ion release, shown alongside the baseline P concentration in the cell culture medium. (E) Cumulative silicon ion release, demonstrating the sustained Si release over time.

proliferation, as Ca is essential for cellular metabolism and osteoblast activity. In contrast, P ion levels gradually exceeded the initial concentration in the medium, potentially supporting initial osteogenic responses and influencing cell viability.

The results revealed that none of the extracts collected from the cement composites in complete cell culture medium showed cytotoxic effects, with viability values higher than 70 % according to the ISO 10993–5:2009 standard. These findings were consistent with the fluorescence images presented in Fig. 9(B), where living cells were observed to be well-attached and spread following treatment with the extracted medium from the samples. On day 1, the viability of cells cultured in BG7-100 extract medium was markedly higher than that of both control and BG0 cements. Additionally, cells cultured in the extract medium of BG7-20 and BG7-38 composites on day 1 exhibited slightly lower viability compared to those of BG9-20 and BG9-38. This pattern correlates with the ion release data, suggesting that higher MBG content and an intermediate particle size (38 µm) in BG9-38 support ion dissolution, which initially enhances cell proliferation. However, the cell viability of α-TCP/MBG composites decreased by approximately 10 % after day 3, with an additional 10–20 % reduction observed between days 7 and 21, particularly in samples with higher silica content, such as BG9-38. This decline aligns with the elevated Si concentrations from the ion release study, indicating that sustained Si release over time may reduce cell viability due to medium saturation effects. Similar findings by Bielby et al. [51] demonstrated that high concentrations of Si, Ca, and P ions can initially stimulate proliferation but may decrease viability over extended incubation periods. The increased ion influx in α-TCP/MBG composites with 9 wt% MBG, especially in samples with smaller particle sizes, may create a saturated medium that influences cell metabolism and viability [34]. Additionally, phase conversion from α-TCP to HAp, as evidenced in phase analysis, indicates that Ca and P ions are gradually incorporated into the mineralized layer, potentially lowering free Ca concentration available for cellular uptake and affecting long-term cell response. In conclusion, these findings indicate that the prepared α-TCP/MBG composites are not cytotoxic and show promising results for further investigation. However, additional research, including direct contact studies, is needed to fully understand the actual effects of the prepared composites on cell viability and metabolism.

4. Conclusion

Incorporating BG into CPCs emerges as a significant strategy for improving bioactivity and degradation rate, as BG possesses the ability to form a direct bond with bone through its bone-like apatite layer on the

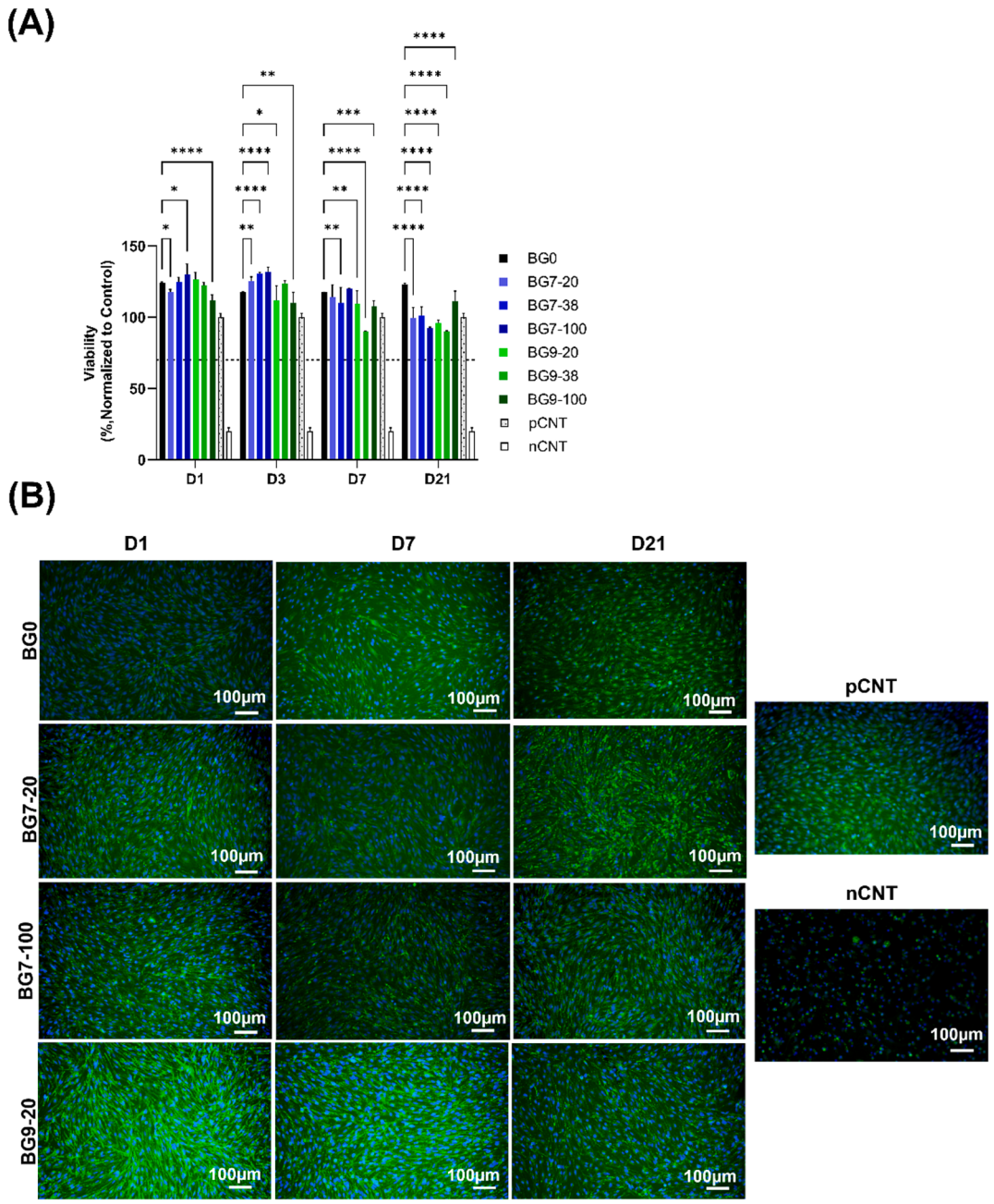

Fig. 9. (A) Cell proliferation of MC3T3-E1 cells cultured with sample extracts collected on days 1, 3, 7, and 21. (B) Fluorescence images showing cell adhesion and growth morphology of MC3T3-E1 cells exposed to extracted medium obtained on days 1, 7, and 21.

surface. Nevertheless, the metabolic mechanism of silicon, a key component of BGs, remains unclear, and determining the optimal amount of BG incorporation or implantation is essential. Consequently, CPCs serve as excellent carriers for such bioactive material, further enhancing their osteopromotive properties. Ongoing research aims to determine the optimal composition and ratio of BG with CPCs. Additionally, the inclusion of BG introduces challenges such as potential changes in handling characteristics and setting kinetics, necessitating careful consideration. In this study, cements containing 7 wt% and 9 wt % 58S MBG with particle sizes of < 20 μm, < 38 μm, and < 100 μm were successfully synthesized, revealing alterations in physicochemical properties compared to BG0 cement, affecting the final setting time, microstructure, mechanical properties, *in vitro* bioactivity and preliminary cell viability.

The particle size of MBG significantly affected the final setting time of the cement composites, with the setting time being ~ 35 min for BG7-20 and ~ 115 min for BG9-20 composites using < 20 μm MBG particles. Despite longer setting times, the compressive strength of < 20 μm α-TCP/MBG composites exceeded that of < 38 μm α-TCP/MBG composites, likely due to differences in porosity. Specifically, <20 μm composites exhibited approximately 64 % and 63 % porosity, whereas < 38 μm composites had higher porosity values around 70 % and 69 %, respectively. These findings suggests that the incorporation of < 20 μm MBG particles results in a denser and more homogeneous microstructure, contributing to improved mechanical stability. Notably, BG7-100 composite samples demonstrated a compressive strength of ~ 0.69 MPa, significantly higher than the BG0 cements (~0.58 MPa), with compressive strength values of α-TCP/MBG composites overall falling within the range of trabecular bone compressive strength (0.22 to 10.44 MPa).

Acellular bioactivity assessment further emphasized the role of MBG content and particle size in modulating bioactivity. The pH initially increased, stabilizing around 6.8 over 21 days, indicating ionic exchange and partial dissolution that aligns with XRD-confirmed phase transformations. BG9-38 (9 wt% MBG, 38 μm) showed the highest cumulative ion release (Ca: 80.4 μg/mL, P: 705.4 μg/mL, Si: 130.4 μg/mL) by day 21, supporting accelerated apatite formation. The < 38 μm particle size optimized ion availability and degradation rate without compromising stability, as shown by increased degradation in BG7-38 and BG9-38. In contrast, BG0 (no MBG) exhibited minimal degradation, underscoring MBG's role in enhancing composite breakdown. The preliminary cell study provided a comprehensive understanding of how dissolution products from α-TCP/MBG composites influenced cellular metabolism. Viability decreased by around 20 % from day 1 to day 21, yet all values remained non-cytotoxic, with over 92 % viability compared to the control group. This was corroborated by the favorable fluorescence images showing that the cells were well-attached and spread. Nevertheless, a more comprehensive cellular assessment needs to be conducted to fully understand how cells could be affected by varying particle sizes and their distribution into cement phases. This observation highlights the intricate interplay between setting kinetics, particle size, and MBG concentration, offering valuable insights into the bioactivity of the α-TCP cement composites.

CRediT authorship contribution statement

Öznur Demir: Writing – original draft, Visualization, Methodology, Investigation, Formal analysis, Data curation, Conceptualization. **Estere Oselska:** Methodology. **Maris Bertins:** Methodology, Formal analysis, Data curation. **Arturs Viksna:** Resources, Methodology, Formal analysis, Data curation. **Aldo R. Boccaccini:** Writing – review & editing, Supervision, Resources. **Dagnija Loca:** Writing – review & editing, Supervision, Resources, Project administration, Conceptualization.

Declaration of competing interest

The authors declare that they have no known competing financial interests or personal relationships that could have appeared to influence the work reported in this paper.

Acknowledgement

The authors acknowledge the financial support for Open Access, the access to the infrastructure and expertise of the BBCE—Baltic Biomaterials Centre of Excellence (H2020 research and innovation programme under grant agreement No. 857287) and the Ministry of Economics of the Republic of Latvia "State research project in the field of biomedicine, medical technologies and pharmacy (BioMedPharm)" No. VPP-EM-BIOMEDICĪNA-2022/1-0001. The authors also express gratitude to Meng Li for invaluable assistance with the initial synthesis of bioactive glass particles.

Appendix A. Supplementary data

Supplementary data to this article can be found online at https://doi.org/10.1016/j.matdes.2024.113463.

Data availability

Data will be made available on request.

References

[1] A.H. Schmidt, Autologous bone graft: Is it still the gold standard? Injury 52 (2021) S18–S22, https://doi.org/10.1016/j.injury.2021.01.043.
[2] W.E. Brown, L.C. Chow, A new calcium-phosphate setting cement, J. Dent. Res. 62 (1983) 672.
[3] R.Z. Legeros, Calcium phosphate materials in restorative dentistry: a review, Adv. Dent. Res. 2 (1988) 164–180, https://doi.org/10.1177/08959374880020011101.
[4] O. Dima, A.C. Didilescu, C.C. Manole, C. Pameijer, C. Călin, Synthetic composites versus calcium phosphate cements in bone regeneration: a narrative review, Ann. Anat. - Anat. Anzeiger. 255 (2024) 152273, https://doi.org/10.1016/j.aanat.2024.152273.
[5] V. Campana, G. Milano, E. Pagano, M. Barba, C. Cicione, G. Salonna, W. Lattanzi, G. Logroscino, Bone Substitutes in Orthopaedic Surgery: from Basic Science to Clinical Practice (2014) 2445–2461, https://doi.org/10.1007/s10856-014-5240-2.
[6] A. D'Onofrio, R.G. Hill, N.W. Kent, S.C.F. Rawlinson, S.A. Shahdad, Development of a novel formulation of bioactive glass based calcium phosphate cement for bone grafting, Adv. Funct. Mater. 2401953 (2024) 1–15, https://doi.org/10.1002/adfm.202401953.
[7] H. Zhao, J. Kang, X. Lian, Y. Song, D. Wang, R. Xu, L. Zhao, D. Huang, B. Niu, The self-regulating on cohesion properties of calcium phosphate/ calcium sulfate bone cement improved by citric acid/sodium alginate, Colloids Surfaces B Biointerfaces. 231 (2023) 113548, https://doi.org/10.1016/j.colsurfb.2023.113548.
[8] L. Degli Esposti, K. Zheng, A. Piancastelli, A.C. Ionescu, A. Adamiano, A. R. Boccaccini, M. Iafisco, Composite materials of amorphous calcium phosphate and bioactive glass nanoparticles for preventive dentistry, Ceram. Int. 50 (2024) 593–602, https://doi.org/10.1016/j.ceramint.2023.10.137.
[9] A. Sadiasa, S.K. Sarkar, R.A. Franco, Y.K. Min, B.T. Lee, Bioactive glass incorporation in calcium phosphate cement-based injectable bone substitute for improved in vitro biocompatibility and in vivo bone regeneration, J. Biomater. Appl. 28 (2014) 739–756, https://doi.org/10.1177/0885328213478256.
[10] M. Kamitakahara, K. Kato, M. Umetsu, K. Yoshihara, Y. Yoshida, Design of bioresorbable calcium phosphate cement with high porosity via the addition of bioresorbable polymers, J. Biomater. Appl. (2024), https://doi.org/10.1177/08853282241277477, 08853282241277477.
[11] R.A. Perez, H.W. Kim, M.P. Ginebra, Polymeric additives to enhance the functional properties of calcium phosphate cements, J. Tissue Eng. 3 (2012) 1–20, https://doi.org/10.1177/2041731412439555.
[12] Ö. Demir-Oğuz, A.R. Boccaccini, D. Loca, Injectable bone cements: What benefits the combination of calcium phosphates and bioactive glasses could bring? Bioact. Mater. 19 (2023) 217–236, https://doi.org/10.1016/j.bioactmat.2022.04.007.
[13] S. Larsson, G. Hannink, Injectable bone-graft substitutes: Current products, their characteristics and indications, and new developments, Injury 42 (2011) S30–S34, https://doi.org/10.1016/j.injury.2011.06.013.
[14] M.J. Coathup, Q. Cai, C. Campion, T. Buckland, G.W. Blunn, The effect of particle size on the osteointegration of injectable silicate-substituted calcium phosphate bone substitute materials, J. Biomed. Mater. Res. - Part B Appl. Biomater. 101 B (2013) 902–910. https://doi.org/10.1002/jbm.b.32895.
[15] R.F. Richter, C. Vater, M. Korn, T. Ahlfeld, M. Rauner, W. Pradel, B. Stadlinger, M. Gelinsky, A. Lode, P. Korn, Treatment of critical bone defects using calcium phosphate cement and mesoporous bioactive glass providing spatiotemporal drug delivery, Bioact. Mater. 28 (2023) 402–419, https://doi.org/10.1016/j.bioactmat.2023.06.001.
[16] H.H.K. Xu, P. Wang, L. Wang, C. Bao, Q. Chen, M.D. Weir, L.C. Chow, L. Zhao, X. Zhou, M.A. Reynolds, Calcium phosphate cements for bone engineering and their biological properties, Nat. Publ. Gr. 5 (2017) 1–19, https://doi.org/10.1038/boneres.2017.56.
[17] M.D. Weir, H.H.K. Xu, Osteoblastic induction on calcium phosphate cement-chitosan constructs for bone tissue engineering, J. Biomed. Mater. Res. A. 94 (2010) 223–233, https://doi.org/10.1002/jbm.a.32665.
[18] J. Noetzel, K. Ozer, B.-H. Reisshauer, A. Anil, R. Rössler, K. Neumann, A. M. Kielbassa, Tissue responses to an experimental calcium phosphate cement and mineral trioxide aggregate as materials for furcation perforation repair: a histological study in dogs, Clin. Oral Investig. 10 (2006) 77–83, https://doi.org/10.1007/s00784-005-0032-1.
[19] R.P. Félix Lanao, S.C.G. Leeuwenburgh, J.G.C. Wolke, J.A. Jansen, Bone response to fast-degrading, injectable calcium phosphate cements containing PLGA microparticles, Biomaterials 32 (2011) 8839–8847, https://doi.org/10.1016/j.biomaterials.2011.08.005.
[20] C. Wu, J. Chang, Mesoporous bioactive glasses: Structure characteristics, drug/growth factor delivery and bone regeneration application, Interface Focus 2 (2012) 292–306, https://doi.org/10.1098/rsfs.2011.0121.
[21] M. Vallet-Regi, A.J. Salinas, Mesoporous bioactive glasses for regenerative medicine, Mater. Today Bio. 11 (2021) 100121, https://doi.org/10.1016/j.mtbio.2021.100121.
[22] L. Yu, Y. Li, K. Zhao, Y. Tang, Z. Cheng, J. Chen, Y. Zang, J. Wu, L. Kong, S. Liu, W. Lei, Z. Wu, A novel injectable calcium phosphate cement-bioactive glass composite for bone regeneration, PLoS One 8 (2013), https://doi.org/10.1371/journal.pone.0062570.
[23] A. El-Fiqi, J.H. Kim, R.A. Perez, H.W. Kim, Novel bioactive nanocomposite cement formulations with potential properties: incorporation of the nanoparticle form of mesoporous bioactive glass into calcium phosphate cements, J. Mater. Chem. B. 3 (2015) 1321–1334, https://doi.org/10.1039/c4tb01634c.
[24] D. Bellucci, A. Sola, V. Cannillo, Hydroxyapatite and tricalcium phosphate composites with bioactive glass as second phase: State of the art and current applications, J. Biomed. Mater. Res. - Part A. 104 (2016) 1030–1056, https://doi.org/10.1002/jbm.a.35619.
[25] M. Karadjian, C. Essers, S. Tsitlakidis, B. Reible, A. Moghaddam, A.R. Boccaccini, F. Westhauser, Biological properties of calcium phosphate bioactive glass composite bone substitutes: current experimental evidence, Int. J. Mol. Sci. 20 (2019) 1–22, https://doi.org/10.3390/ijms20020305.

[26] M. Dadkhah, L. Pontiroli, S. Fiorilli, A. Manca, F. Tallia, I. Tcacencu, C. Vitale-Brovarone, Preparation and characterisation of an innovative injectable calcium sulphate based bone cement for vertebroplasty application, J. Mater. Chem. B. 5 (2017) 102–115, https://doi.org/10.1039/c6tb02139e.
[27] L.S. Mendes, S. Saska, F. Coelho, T.S.D.O. Capote, R.M. Scarel-Caminaga, R. Marchetto, R.G. Carrodeguas, A.M.M. Gaspar, M.A. Rodríguez, Injectable β-TCP/MCPM cement associated with mesoporous silica for bone regeneration: Characterization and toxicity evaluation, Biomed. Mater. 13 (2018), https://doi.org/10.1088/1748-605X/aa9085.
[28] W. Cao, Y. Peng, Y. Zhang, F. Qiu, M. Li, J. Tang, Z. Wu, Novel bone wax based on tricalcium silicate cement and BGs mixtures, Biomed. Mater. 13 (2018) 65001, https://doi.org/10.1088/1748-605x/aad73c.
[29] W. Cao, S. Zong, Y. Zhang, F. Qiu, J. Tang, Z. Wu, J. Luan, Preparation of a novel bone wax with modified tricalcium silicate cement and BGs, Mater. Sci. Eng. C. 99 (2019) 979–985, https://doi.org/10.1016/j.msec.2019.02.049.
[30] Z. Pu, H. Fan, C. Zhang, C. Gao, P. Zhu, Effect of bioglass on in vitro bioactivity and cytocompatibility of biphasic α-tricalcium phosphate/gypsum cements, Mater. Technol. 00 (2020) 1–12, https://doi.org/10.1080/10667857.2020.1761654.
[31] C. Li, W. Hao, C. Wu, W. Li, J. Tao, F. Ai, H. Xin, X. Wang, Injectable and bioactive bone cement with moderate setting time and temperature using borosilicate bioglass-incorporated magnesium phosphate, Biomed. Mater. 15 (2020), https://doi.org/10.1088/1748-605X/ab633f.
[32] Z. Wu, Z. Lin, A. Yao, S. Ye, H. Pan, X. Cui, D. Wang, Influence of particle size distribution on the rheological properties and mathematical model fitting of injectable borosilicate bioactive glass bone cement, Ceram. Int. 46 (2020) 24395–24406, https://doi.org/10.1016/j.ceramint.2020.06.222.
[33] H. Mabroum, H. Noukrati, H. Ben, H. Oudadesse, A. Barroug, The effect of bioactive glass particle size and liquid phase on the physical-chemical and mechanical properties of carbonated apatite cement, Ceram. Int. 48 (2022) 28207–28220, https://doi.org/10.1016/j.ceramint.2022.06.126.
[34] Ö. Demir, A. Pylostomou, D. Loca, Octacalcium phosphate phase forming cements as an injectable bone substitute materials: preparation and in vitro structural study, Biomater. Adv. 157 (2024), https://doi.org/10.1016/j.bioadv.2023.213731.
[35] P. Sepulveda, J.R. Jones, L.L. Hench, In vitro dissolution of melt-derived 45S5 and sol-gel derived 58S bioactive glasses, J. Biomed. Mater. Res. 61 (2002) 301–311, https://doi.org/10.1002/jbm.10207.
[36] L.L. Li, R. Clark, A.E. Hench, An investigation of bioactive glass powders by sol-gel processing, J. Appl. Biomater. 2 (1991) 231–239.
[37] C. Nan Li, C. Jiang, X. Zhang, X. Gb, J. Zhang, Y. Yuan, Y.L. Liu, J. Shi, J. Wang, Preparation of rhBMP-2 loaded mesoporous bioactive glasses/calcium phosphate cements porous composite scaffold for rapid bone tissue regeneration, J. Mater. Chem. B. 3 (2015) 8558. https://doi.org/10.1039/C5TB01423A.
[38] T. Kokubo, H. Takadama, How useful is SBF in predicting in vivo bone bioactivity? Biomaterials 27 (2006) 2907–2915, https://doi.org/10.1016/j.biomaterials.2006.01.017.
[39] D. Loca, M. Sokolova, J. Locs, A. Smirnova, Z. Irbe, Calcium phosphate bone cements for local vancomycin delivery, Mater. Sci. Eng. C. 49 (2015) 106–113, https://doi.org/10.1016/J.MSEC.2014.12.075.
[40] N. Doebelin, R. Kleeberg, Profex: a graphical user interface for the Rietveld refinement program BGMN, J. Appl. Crystallogr. 48 (2015) 1573–1580, https://doi.org/10.1107/S1600576715014685.
[41] M. Schumacher, P. Habibovic, S. van Rijt, Mesoporous bioactive glass composition effects on degradation and bioactivity, Bioact. Mater. 6 (2021) 1921–1931, https://doi.org/10.1016/j.bioactmat.2020.12.007.
[42] D.H. Everett, Manual of symbols and terminology for physicochemical quantities and units, appendix ii: definitions, terminology and symbols in colloid and surface, Chemistry 31 (1972) 577–638, https://doi.org/10.1351/pac197231040577.
[43] A. López-Noriega, D. Arcos, I. Izquierdo-Barba, Y. Sakamoto, O. Terasaki, M. Vallet-Regí, Ordered mesoporous bioactive glasses for bone tissue regeneration, Chem. Mater. 18 (2006) 3137–3144, https://doi.org/10.1021/cm060488o.
[44] I. Kovrlija, J. Locs, D. Loca, Octacalcium phosphate: Innovative vehicle for the local biologically active substance delivery in bone regeneration, Acta Biomater. 135 (2021) 27–47, https://doi.org/10.1016/j.actbio.2021.08.021.
[45] N. Miyatake, K.N. Kishimoto, T. Anada, H. Imaizumi, E. Itoi, O. Suzuki, Effect of partial hydrolysis of octacalcium phosphate on its osteoconductive characteristics, Biomaterials 30 (2009) 1005–1014, https://doi.org/10.1016/j.biomaterials.2008.10.058.
[46] A. Sugawara, K. Asaoka, S.J. Ding, Calcium phosphate-based cements: clinical needs and recent progress, J. Mater. Chem. B. 1 (2013) 1081–1089, https://doi.org/10.1039/c2tb00061j.
[47] M.P. Ginebra, F.C.M. Driessens, J.A. Planell, Effect of the particle size on the micro and nanostructural features of a calcium phosphate cement: a kinetic analysis, Biomaterials 25 (2004) 3453–3462, https://doi.org/10.1016/j.biomaterials.2003.10.049.
[48] Q. Zhang, Y. Leng, R. Xin, A comparative study of electrochemical deposition and biomimetic deposition of calcium phosphate on porous titanium, Biomaterials 26 (2005) 2857–2865, https://doi.org/10.1016/j.biomaterials.2004.08.016.
[49] L. Stipniece, A. Ramata-Stunda, J. Vecstaudza, I. Kreicberga, D. Livkisa, A. Rubina, A. Sceglovs, K. Salma-Ancane, A comparative study on physicochemical properties and in vitro biocompatibility of Sr-substituted and Sr ranelate-loaded hydroxyapatite nanoparticles, ACS Appl. Bio Mater. 6 (2023) 5264–5281, https://doi.org/10.1021/acsabm.3c00539.
[50] K.A. Hageman, R.L. Blatt, W.A. Kuenne, R.K. Brow, T.E. McIff, Effect of pH and hydroxyapatite-like layer formation on the antibacterial properties of borophosphate bioactive glass incorporated poly(methyl methacrylate) bone cement, Front. Bioeng. Biotechnol. 12 (2024) 1–12, https://doi.org/10.3389/fbioe.2024.1462795.
[51] R.C. Bielby, I.S. Christodoulou, R.S. Pryce, W.J.P. Radford, L.L. Hench, J.M. Polak, Time- and concentration-dependent effects of dissolution products of 58S sol-gel bioactive glass on proliferation and differentiation of murine and human osteoblasts, Tissue Eng. 10 (2004) 1018–1026, https://doi.org/10.1089/ten.2004.10.1018.